https://dx.doi.org/10.1016/j.apenergy.2022.119464

Effects of methane steam reforming on the mechanical stability of solid oxide fuel cell stack

Meiting Guo[1,2], Xiao Ru[1], Lin Yang[1], Meng Ni[2*], Zijing Lin[1*]

1) Department of Physics, Hefei National Laboratory for Physical Sciences at the Microscale, University of Science and Technology of China, Hefei, China

2) Department of Building and Real Estate, Research Institute for Sustainable Urban Development (RISUD) and Research Institute for Smart Energy (RISE), The Hong Kong Polytechnic University, Hung Hom, Kowloon, Hong Kong, China

ABSTRACT

Thermal stress-induced mechanical failure is a critical issue for practical application of solid oxide fuel cells (SOFCs). Due to the lack of study on the thermo-mechanical behavior of SOFC with different methane steam pre-reforming ratios (R), a 3D thermo-mechanical model is developed to systematically evaluate the mechanical performance of SOFC running on methane fuel. The model fully considers the coupled transport and reaction processes in the SOFC. The numerically obtained temperature is imported to a mechanical sub-model to determine the thermal stress and strain of SOFC components under various operating conditions, namely with different R values. Covering all R conditions, glass-ceramic sealant is the most dangerous component, while cathode is in sub-critical state. When R<0.4, the electrolyte has the minimum failure probability. When R>0.4, the anode becomes the safest component in SOFC stack. With the increase of R, the failure probability of anode decreases all the way and always stays in the safe range, while first decreases then increases for electrolyte, cathode and sealant. R within 0.4-0.7 is favorable for the reliability of the whole SOFC stack. This study is useful for identifying optimal operating conditions for efficient and stable operation of SOFC running on alternative hydrocarbon fuels.

Keywords: Solid oxide fuel cell stack; Multiphysics coupling; Pre-reforming ratio; Failure probability.

1. Introduction

Solid Oxide Fuel Cell (SOFC) is a promising electrochemical conversion device which can convert chemical energy of fuels into electrical energy directly. As an innovative energy conversion technology to replace conventional thermal power plants, SOFC has various advantages such as high energy conversion efficiency, high volumetric power density, less or no pollution, and fuel flexibility. Although significant progress has been made in new material development to achieve high performance of SOFC button cell and one-cell SOFC stack, the performance of practical SOFC stacks with multiple cells is still quite low. This is mainly due to highly uneven gas distribution in the SOFC stack and the additional ohmic loss caused by current collection. In addition to lower performance, practical SOFC stacks are more mechanically fragile as the failure of any cell can cause the failure of the entire stack. Therefore, for practical application of SOFC, it is of paramount importance to improve the performance and durability of SOFC stacks.

Due to the transport of oxygen ions from the cathode to the anode side through the dense electrolyte, in principle SOFCs are capable of running on any combustible fuels, including methane, ammonia, or even solid carbon. The direct use of methane (CH_4) in SOFC has received extensive attention in recent years as methane is a key component of natural gas and biogas [1]. Moreover, CH_4 can also be obtained from liquid hydrocarbon fuels through various chemical processes [2]. However, as direct electrochemical oxidation of CH_4 in SOFC is very challenging and requires novel catalysts, CH_4 is first converted to H_2 and CO by internal or external methane steam reforming reaction (MSR). Then the produced CO and H_2 are diffused to the triple phase boundary (TPB) near the anode-electrolyte interface to take part in electrochemical reaction for

electricity generation. As the MSR is endothermic while the electrochemical processes and overpotential losses in SOFC generate heat, it is ideal to make use of the heat generation from SOFC for internal MSR (IMSR), which can take place in the nickle-yttria stabilized zirconia (Ni-YSZ) anode. However, SOFC stack with IMSR may suffer from large temperature gradient, which in turn may cause large thermal stress and reduce the mechanical stability of SOFC components. Moreover, thermal cracking of CH_4 or CO in the porous Ni-based anode can cause carbon deposition, which can fill in the pores, impede gas transport, cover the reaction sites, and eventually cause performance degradation. External MSR (EMSR) can avoid carbon deposition. However, it needs extra heat and reactor, which decrease the overall efficiency of SOFC system. Thus, partial EMSR and partial IMSR seem to be a feasible way of achieving both high performance and good durability of SOFC stack. Although some preliminary research works have been done to understand the effects of methane steam pre-reforming ratios on the system performance, the effects of methane steam pre-reforming ratio (R) on the thermomechanical behaviors of practical SOFC stack have not been studied yet.

Until now, there have been only limited studies on thermomechanical behaviors of SOFC stacks with a variety of assumptions and simplifications. For example, Anandakumar et al. [3] studied the influence of graded electrode layers on thermal stress and failure probability of a button cell. The research was carried out based on isothermal field and an assumed linear temperature distribution. Lin et al. [4, 5] investigated the influence of sealing method on stress distribution of a 3-cell stack, the PEN structure is considered as a whole without considering property difference of different components. However, the mechanical properties of anode, electrolyte and cathode are vastly different [6]. The property discontinuity of components exerts tremendous influence on stress distribution at the interface between adjacent components, and the thermal stress induced by mismatch of thermal expansion coefficient can’t be ignored [7]. Peksen [8] conducted the research about the stress and strain distribution of the production-scale 36-cell

SOFC stack with thermal field acquired by averaging heat source inside stack, which may underestimate the temperature difference and overestimate the mechanical stability of stack. It should be noted that the temperature difference inside the SOFC stack cannot be ignored, especially for large-scale stack with internal methane steam reforming [9]. To reduce the requirement for computation resources, Frandsen et al. [10] developed a homogenization model to study the mechanical performance of SOFC stack with high computation efficiency. The average stress is calculated and the mapping relationship between average stress and local fracture failure is used to evaluate the safety of SOFC stack. However, this method adopted a lot of simplifications, which makes the actual details of stress distribution hardly to be captured. In general, the mechanical modeling of large-scale SOFC stack with maximum possible rigor is desirable for many design and optimization purposes.

To our knowledge, the mechanical performance analysis for large-scale stack is very limited. No study has been conducted for stack with high geometry resolution and with different R. As mentioned earlier, partial pre-reforming of methane is preferred for practical SOFC stack to achieve high system performance. Therefore, a fundamental understanding on how the R value affect the thermo-mechanical stability of SOFC is of practical importance to identify suitable operating conditions to achieve both high performance and good durability of SOFC stack. In this study, thermo-mechanical model is developed to evaluate thermal-stress and strain distribution of a 15-cell SOFC stack with different R for the first time. Thermal stress distribution characteristics of all the components of SOFC stack are clearly analyzed and the underlying mechanism is revealed. Based on the stress distribution, the mechanical failure probability of different components of the SOFC stack can be obtained. Parametric simulations are conducted to investigate the effects of R on the performance and mechanical stability of the SOFC stack, which are critical for the development of high performance and durable SOFC stacks.

2. Models and method

2.1 Geometry structure, grid setting and working condition

Fig. 1a and Fig. 1b display the geometry of a 15-cell SOFC stack and the detailed structure of a repeating unit. The repeating unit of SOFC stack includes: nickle-8% mol yttria stabilized zirconia (Ni-YSZ) anode, yttria stabilized zirconia (YSZ) electrolyte and strontium-doped lanthanum manganite-yttria stabilized zirconia (LSM-YSZ) cathode, manifolds, channels, sealants (Glass-Ceramic) and frames/interconnectors (Crofer 22 APU). The cell periphery and the window-frame are bonded by glass-ceramic seal. The overall stack size corresponds to length/width/height=135/100.5/62.5 (mm), with an active area of 10 cm × 10 cm. The thicknesses of fuel/air sub-channels, anode, electrolyte, cathode, and inter-connector (IC) are 1mm, 1 mm, 10 μm, 90 μm, and 2 mm. The width of sub-channel and rib is 2.5 mm and 1.5 mm, respectively. Both the fuel and air inlets/outlets in manifold have the same size: 5.5 mm × 5.5 mm. To avoid backflow, the inlet/outlet channels are extended 30 mm outwards as displayed in Fig. 1a. The outer edge of frames is 2 mm wide. The upper and lower edges of PEN sealant are 1 mm wide, and the side edge is 1.5 mm wide, while the height of PEN sealant is the same as that of PEN. This stack is based on the 2-in-3-out counter-flow pattern, because counter-flow SOFC has demonstrated maximum electric output compared with co-flow and cross-flow stack [11, 12]. Half of the structure is constructed due to the symmetry of the stack (Fig. 1a), which can significantly reduce the demand on computational resource without losing accuracy. Detailed components of one repeating cell is shown in Fig. 1b. The details of grid setting for multiphysics coupling model can be found in our recent publication [13]. The stack model for thermo-mechanical analysis is meshed with the SOLID186 20-node hexahedral elements. Grid independence test is conducted for thermal stress-strain calculation, and a total grid number of 512 thousand is chosen for thermo-mechanical model.

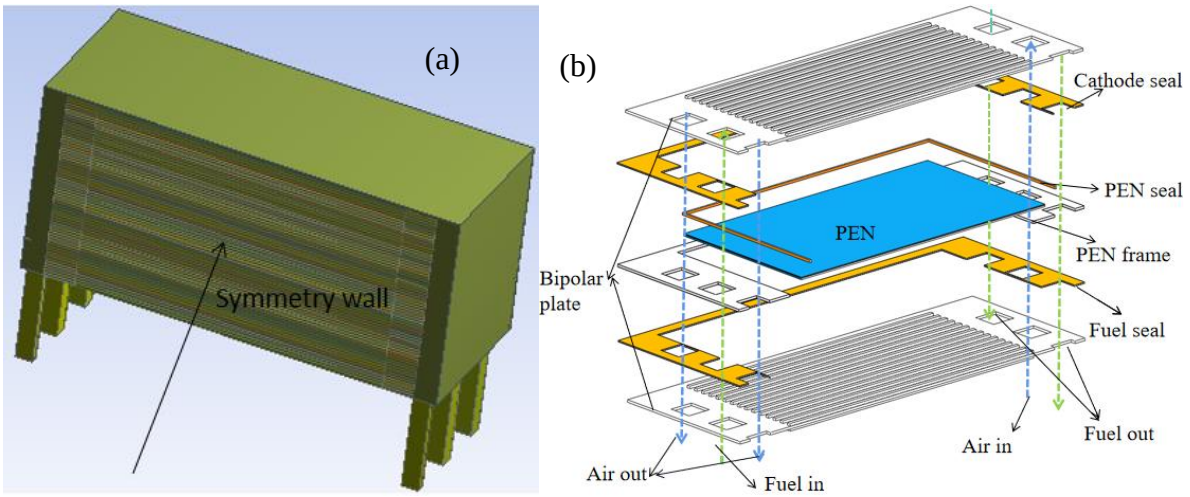

Fig. 1. (a) Geometry of a 2-in-3-out 15-cell stack; (b) Detailed structure of the repeat cell layer.

According to the previous research [14], carbon deposition in SOFC can be safely prevented when the molar ratio of H_2O to CH_4 is larger than 2. The H_2O/CH_4 ratio is chosen to be 2 as the base case, denoted as R=0, which means there is no external methane steam reformation. Only methane steam reforming reaction and water gas shift reaction (WGS) are considered in the external reformer, and the equilibrium reaction model is employed for WGS reaction. The operating conditions of external reformer are assumed to be controlled to provide the required R [15]. There has been experiment research [16, 17] that introduce the experiment control process of external methane steam reforming in detail, which implies the aforementioned working conditions attainable. After the methane fuel passing through the reformer, the reformed fuel is heated by heat exchanger [15] or electrical heater [18] or some other means before entering into the SOFC stack. The inlet temperature of fuels supplied to the stack is controlled at 700 ℃ for all R conditions. The composition mole fractions and velocities of inlet fuel are adjusted according to the change of R. The fuel compositions and the flow velocities at the stack fuel inlet, together with the power outputs of the SOFC stack are summarized in Table 1. Even though different fuels are considered, it is noted that this is a steady-state analysis and does not involve transient state modeling.

As the H_2O/CH_4 ratios are always larger than 2, the carbon deposition is not considered for

all the cases studied. The fuel utilization is 70%, and the oxygen utilization of the air flow is 33.3%. The high oxygen utilization used here is for the benefit of potentially high system efficiency in real applications and has been examined experimentally by different groups [19, 20]. The output current density is fixed as 4000A/m^2. Both the inlet temperatures of fuel and air flow are 700 ℃. The Ni content of anode and LSM content of cathode are both 50%, and the porosity of electrodes are both 0.4.

Table 1 Fuel molar compositions, flow velocities at the stack fuel inlet (V_{fuel}) and the power outputs of the SOFC stack operating at 700 ℃.

R	H_2 (%)	H_2O (%)	CH_4 (%)	CO (%)	CO_2 (%)	V_{fuel} (m/s)	Power output (W)
0	0	66.650	33.350	0	0	4.394	415.2
0.2	22.235	48.353	23.530	1.294	4.588	4.982	430.2
0.4	37.947	35.735	15.789	4.158	6.369	5.567	442.2
0.6	49.524	26.666	9.524	7.619	6.667	5.859	453.6
0.8	58.370	19.891	4.348	11.196	6.195	6.738	467.4
1	65.346	14.654	0	14.654	5.346	7.324	481.2

2.2 Thermo-mechanical stress and strain model

The multiphysics coupling models are built with the commercial software FLUENT®, combined with user-developed subroutines. The methodology details of the multiphysics model can be referred to our previous work [9, 13]. The thermo-mechanical model is developed based on the multiphysics coupling models. That is, the temperature field obtained through the multiphysics modeling is imported into the structural mechanical model for the ensuing mechanical analysis, thus realizing the one-way thermo-mechanical coupling process.

The total strain of one material is expressed as:

$$\varepsilon = \varepsilon_0 + \varepsilon_{el} + \varepsilon_{th} + \varepsilon_{cr} + \varepsilon_{pl} \quad (1)$$

Here, ε_0, ε_{el} and ε_{th} represent the initial strain, elastic strain and thermal strain, respectively. ε_{cr} and ε_{pl} are creep strain and time-independent plastic strain, which are irreversible strain.

The thermal strain is formulated as:

$$\varepsilon_{th} = \int_{T_{ref}}^{T} a(T)\,\mathrm{d}T \tag{2}$$

Where a, T_{ref} and T denote thermal expansion coefficient (TEC), reference temperature and the absolute temperature. According to the recent experiment study [21], all stresses of the anode support disappeared after reducing NiO-YSZ to Ni-YSZ at 800 ℃. Moreover, 800 ℃ is also usually the stack assembly temperature [8]. Hence, T_{ref} = 800 ℃ is used for all the stack component materials.

In the temperature variation range (about within 200 K) of SOFC stack, it is safe to assume that thermal expansion coefficient is invariable, which is reasonable according to the open literature [22]. Hence,

$$\boldsymbol{\varepsilon}_{th} = a(T - T_{ref}) \tag{3}$$

According to the theory of elasticity, the stress-strain relationship can be expressed as:

$$\boldsymbol{\sigma} = \boldsymbol{D}\boldsymbol{\varepsilon}_{el} + \boldsymbol{\sigma}_0 = \boldsymbol{D}(\boldsymbol{\varepsilon}_t - \boldsymbol{\varepsilon}_{cr} - \boldsymbol{\varepsilon}_{th}) \tag{4}$$

where $\boldsymbol{\sigma}$, $\boldsymbol{D}$ and $\boldsymbol{\sigma}_0$ denote the stress tensor, elasticity matrix and the initial stress, respectively. Based on the generalized Hooke's law of the elastic isotropic materials, considering the influence of temperature distribution, the stress-strain relationship can be expressed as:

$$\begin{pmatrix} \sigma_x \\ \sigma_y \\ \sigma_z \\ \sigma_{xy} \\ \sigma_{yz} \\ \sigma_{zx} \end{pmatrix} = \frac{E}{(1+\nu)(1-2\nu)} \begin{bmatrix} 1-\nu & \nu & \nu & 0 & 0 & 0 \\ \nu & 1-\nu & \nu & 0 & 0 & 0 \\ \nu & \nu & 1-\nu & 0 & 0 & 0 \\ 0 & 0 & 0 & \frac{1-2\nu}{2} & 0 & 0 \\ 0 & 0 & 0 & 0 & \frac{1-2\nu}{2} & 0 \\ 0 & 0 & 0 & 0 & 0 & \frac{1-2\nu}{2} \end{bmatrix} \begin{pmatrix} \varepsilon_x \\ \varepsilon_y \\ \varepsilon_z \\ 2\varepsilon_{xy} \\ 2\varepsilon_{yz} \\ 2\varepsilon_{zx} \end{pmatrix} - \frac{Ea\Delta T}{1-2\nu} \begin{pmatrix} 1 \\ 1 \\ 1 \\ 0 \\ 0 \\ 0 \end{pmatrix} \tag{5}$$

Where $\boldsymbol{E}$ represents Young's modulus and ν denotes Poisson's ratio. $\boldsymbol{\sigma_x}$, $\boldsymbol{\sigma_y}$, $\boldsymbol{\sigma_z}$ and $\boldsymbol{\varepsilon_x}$, $\boldsymbol{\varepsilon_y}$, $\boldsymbol{\varepsilon_z}$ are the normal stress and strain values. $\boldsymbol{\sigma_{xy}}$, $\boldsymbol{\sigma_{yz}}$, $\boldsymbol{\sigma_{zx}}$ and $\boldsymbol{\varepsilon_{xy}}$, $\boldsymbol{\varepsilon_{yz}}$, $\boldsymbol{\varepsilon_{zx}}$ are the shear stress and strain values, respectively. ΔT refers to the temperature difference between the actual temperature and the

reference temperature.

The boundary conditions for the thermal mechanical model include: (1) tightly bonded PEN without slip among the components, (2) slight sliding and no gap allowed between the electrode and interconnector (IC), (3) sealant tightly bonded with cell and frame (rigid sealed stack), (4) no force applied on the outer surface of the stack, (5) The bottom of the whole stack is frictionless supported. The 3D structural thermo-mechanical model, together with the boundary conditions, is solved by the sparse matrix direct solver of the commercial finite element software ANSYS 15.0.

2.3 Effective mechanical property model

The composite sphere method for the heterogeneous material [23] is used to calculate the bulk modulus ($\boldsymbol{K_{com}}$) and shear modulus ($\boldsymbol{G_{com}}$) of dense composite material:

$$K_{com} = K_2 + \frac{\varphi_1}{1/(K_1 - K_2) + 3\varphi_2/(3K_2 + 4G_2)} \tag{6}$$

$$G_{com} = G_2 + \frac{\varphi_1}{1/(G_1 - G_2) + 6\varphi_2(K_2 + 2G_2)/5(G_2(3K_2 + 4G_2))} \tag{7}$$

where $\boldsymbol{K_i}$ and $\boldsymbol{G_i}$ are respectively the bulk and shear modulus of component i in the composite electrode. φ_i is the volume fraction of phase i in the composite electrode. The results of Eq. 6 and Eq. 7 depend on which material phase is chosen as the matrix or the impurity, but the difference is generally small [24]. The higher values are used here.

The effective Young's modulus ($\boldsymbol{E_{eff}}$) and shear modulus ($\boldsymbol{G_{eff}}$) for the porous electrode material are given by the models developed by Ramakrishnan and Arunachalam [25]:

$$E_{eff} = E_0 \frac{(1-\psi)^2}{1+(2-3\nu_0)\psi} \tag{8(}$$

$$G_{eff} = G_0 \frac{(1-\psi)^2}{1+(11\text{-}19\nu_0)/(4+4\nu_0)\psi} \tag{9}$$

Here, $\boldsymbol{E_0}$ and v_0 are respectively the Young's modulus and Poisson's ratio of the dense composite material. Ψ denotes porosity of a porous electrode.

The TEC of the composite material is formulated as [26, 27]:

$$a_{com} = \sum_i a_i \varphi_i + 4\frac{G_m}{K_c}\sum_i \frac{K_c - K_i}{4G_m + 3K_i}(a_m - a_i)\varphi_i \tag{10}$$

Where i, c and m represent element, composite and matrix, respectively.

2.4 Failure probability analysis model

Due to the brittle nature, ceramic component usually fails due to a significant flaw at a high tensile stress. The mechanical strength of ceramic materials is statistically distributed due to the statistical distribution of material flaws and defects induced by the manufacturing process. The strength of ceramic component is also size dependent [28], because a larger volume of material may contain more stress triggers. To this regard, the Weibull statistical analysis method is widely used to estimate the failure probability of brittle SOFC components caused by tensile stresses [3, 29, 30]. The failure probability of brittle component j is calculated as:

$$P_{f,j} = 1 - \prod_{x=1}^{3} \exp\left(-\int \left(\frac{\sigma_{j,x}}{\sigma_0}\right)^m \frac{dV_j}{V_0}\right) \tag{11}$$

Here, σ_0, m and V_0 are the characteristic strength, Weibull modulus and reference volume, respectively. V_j is the volume of component j, x denotes the component of principal stress. Material is generally considered to be safe when failure probability is less than 1E-6 from an engineering perspective [7].

2.5 Model verification

The multiphysics coupling model has been validated by its capability of reproducing the experimental I-V result and temperature distribution of an experiment stack, as illustrated in Fig. 2 of Ref. [13]. The ability to provide temperature distributions in agreement with experimental data is an important advantage of this study as mechanical problems are strongly influenced by the temperature fields.

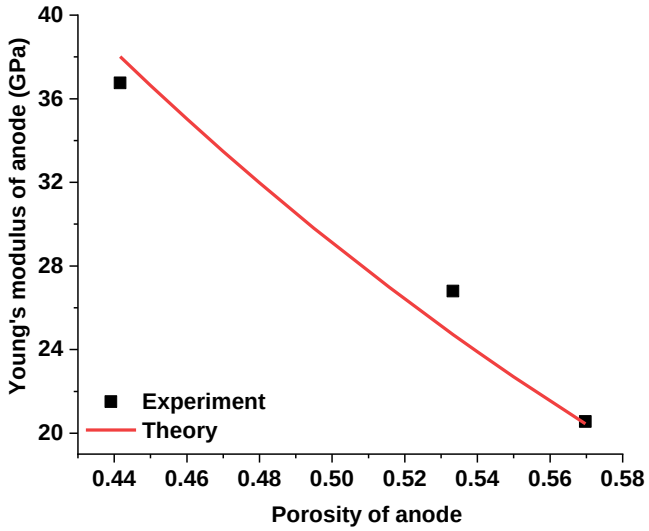

Fig. 2. Comparison of theoretical and experimental Young's modulus of Ni-YSZ anode

To validate the effective mechanical property model, the Young's modulus values of anode predicted by mechanical model have been compared with the result of experiment [31]. It can be seen from Fig. 2 that the theoretical result agrees well with the experiment results for the whole porosity range of interest, justifying the mechanical property models used here.

X-ray diffraction (XRD) is generally used to measure the strain of a material, then X-ray elastic constants can be used to convert the measured strain value to stress [32]. The mechanical model and the mechanical properties of components have been tested by computing the residual stress of an experimental half-cell [33], with an anode layer of 1.5 mm and an electrolyte layer of 10 um. The calculated compressive stress of the electrolyte is 548 MPa at room temperature, in excellent agreement with the experimentally measured result of 560 ± 35 MPa. The predictive power of the mechanical models is thus confirmed.

Table 2 Mechanical parameters of dense material.

Materials	Young's modulus (GPa)	Poisson's ratio	TEC (1E-6/K)
Ni (25℃)	200 [34]	0.313 [35]	16.9 [26]
Ni (800℃)	171 [36]	0.313	16.9 [27]

YSZ (25℃)	215 [37]	0.317 [37]	10.3 [38]
YSZ (800℃)	185 [37]	0.317	10.3
LSM	95 [39]	0.32 [40]	12.4 [41]
Glass-ceramic seal	linear interpolation with 64@600℃ & 16@800℃ [22]	0.28 [22]	11.1 [22]
Frame/IC	linear interpolation with 184@550℃,124@650℃, 92@750℃, 48@850℃ [5]	0.3 [42]	11.5 [42]

Table 3 Weibull parameters.

Materials	m	σ_0	V_0 (mm^3)
Anode (Ni/8YSZ) (800℃) [43]	14.5	124	0.73
Electrolyte (YSZ) (800℃) [44]	8.0	282	0.27
Cathode (LSM) (800℃) [29]	4.0	75	2.81
Glass-ceramic [45]	6.0	34	1

A set of standard structural mechanical models with properly chosen material properties are used to obtain the stress distributions of a 15-cell planar SOFC stack. The mechanical property parameters of dense materials at room temperature and 800℃ are listed in Table 2. The mechanical properties of porous composite electrode can be calculated by effective mechanical property models. The change of Young's modulus of PEN within SOFC operating temperature range (600-800℃) is ignored according to literatures [42, 46]. The temperature dependence of Possion's ratio and thermal expansion coefficient in the usual SOFC operating temperature range can be ignored according to previous research [22]. However, the Young's modulus of Crofer 22 APU frames/ICs and Glass-ceramic sealant are strongly temperature dependent [5, 22], so the temperature dependence of Young's modulus of sealant and frames/ICs are considered. The Weibull parameters used to calculate failure probability of brittle components of SOFC stack are listed in Table 3. As shown in Tables 2 and 3 and references therein, the mechanical parameters of

SOFC components used in this study are based on experimentally measured values for as far as possible.

3. Results and discussion

3.1 The necessity of high geometry resolution for stress calculation of SOFC stack

Generally, anode withstands tensile stress while electrolyte bears compressive stress due to the larger (smaller) volume and TEC of anode (electrolyte) [37, 40], cathode sustains either compressive or tensile stress due to the overlap of TEC range to that of anode [44]. However, the stress state also strongly relies on the temperature distribution and constrain condition from adjacent components [38, 45, 47], the change of thermal load and constrain state can change the stress from tensile state to compressive state, or vice versa. To better reflect the interaction of different components in a cell, the comparative study has been conducted by taking the maximum principal stress as a comparison criterion. SOFC is loaded by the volume-averaged temperature 688 ℃ of one IMSR single-cell stack. The maximum principal stress along the PEN central line in height direction has been displayed in Fig. 3. The stress distribution characteristic of sole PEN as shown in Fig. 3 is consistent with the previous numerical studies [29, 47]. With the increase of adjacent constraint, the freedom for PEN to deform decreases, the stress tends to increase. As shown in Fig. 3, when the contraction of PEN is restrained by sealant, the tensile stress of PEN increases while compressive stress releases. However, the effect of sealant is relatively minor, because the Young's modulus of sealant decreases sharply when temperature increases to 688 ℃. When the frame with relatively higher strength is added outside the sealant, the constraint of PEN is enhanced, and the tensile stress of PEN increases drastically. It should be noted that the addition of IC directly changes the stress of anode outer face from compressive stress to tensile stress. When free PEN is loaded by uniform temperature lower than the reference temperature, the outer surface of anode withstands compressive stress, which is in accordance with the reported

simulation results [29, 42]. However, when the contraction is hindered by IC, the outer surface withstands tensile stress. It was also reported that stress gradient along anode height direction is linked to bending behavior [29]. As discussed above, the previous research solely on the PEN mechanical performance may overestimate the reliability of SOFC. The accurate prediction of stress distribution of SOFC stack should consider the constrain of the neighboring components such as the PEN seal, frame and the bipolar plates.

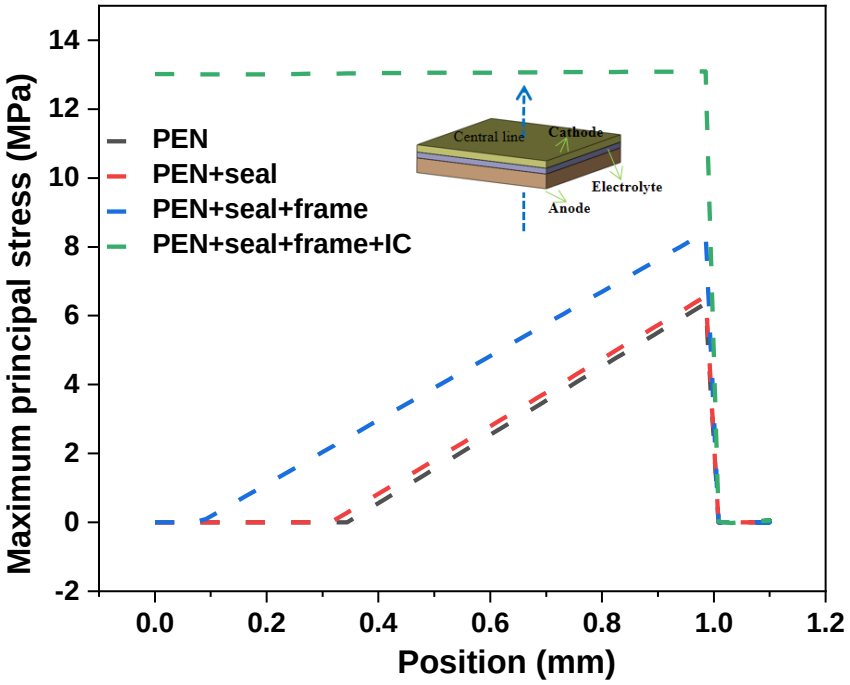

Fig. 3. The maximum principal stress along the PEN central line (the inset dashed arrow line)

3.2 Thermal load

Different R means different ratio of chemical reaction to electrochemical reaction inside SOFC stack, thus leading to different temperature distribution. Fig. 4 shows the stack temperature distributions for three representative R-cases. Notice that the cell stacking directions shown in Fig. 4 and Fig. 1 are different, differ by a rotation of about 90˚. As can be seen from Fig. 4, the internal reforming reaction significantly consumes the heat generated in the SOFC, leading to lower average temperature of the SOFC stack. Without any external reforming, the lowest and the

highest temperature in SOFC stack are 614 ℃ and 747 ℃, respectively. When partial external reforming is considered, the average temperature of SOFC is increased significantly, the lowest temperature is increased to 658 ℃ while the highest temperature increases slightly toward 750 ℃. With complete external reforming, the lowest and highest temperatures of the SOFC stack are increased to 746 ℃ and 876 ℃, respectively.

In addition to the apparent R factor, the stack temperature distribution is also affected by the gas flow uniformity. Based on the flow uniformity definition of Ref. [48], the fuel flow uniformity is calculated to be 86%, 89% and 91% for R = 0, 0.4 and 1, respectively. The flow non-uniformity contributes to the difference in the temperature distribution of different stack cells, as seen in Fig. 4.

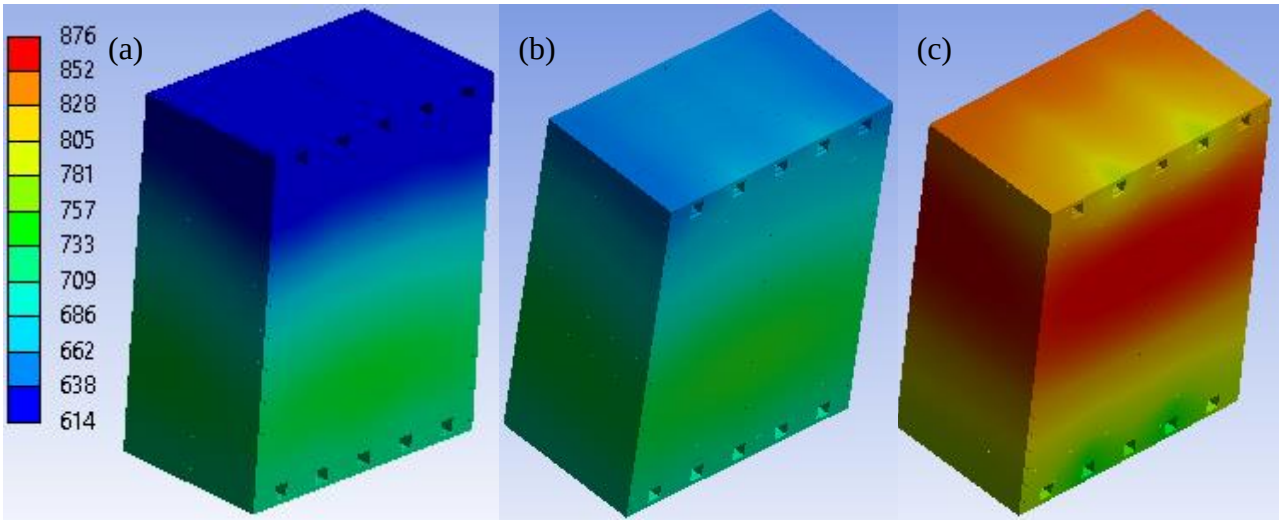

Fig. 4. Temperature (℃) distribution of: (a) IMSR stack; (b) PMSR stack with R=0.4; (c) EMSR stack.

3.3 The influence of temperature gradient on stress distribution and mechanical failure

For SOFC stacks studied in this research, the geometric structure, material property, constraint condition and contact type are all the same, the only difference is the thermal load. Different R means different thermal loads for thermal-mechanical performance analysis of SOFC

stack. The influence of temperature gradient on long-term mechanical performance evolution of a single-cell stack was studied in our previous research [24]. In this study, the influence of temperature gradient on the specific stress distribution details of the 15-cell stack is clearly illustrated by comparing stack loaded by volume-averaged temperature of IMSR stack and temperature distribution of the IMSR stack.

As the tensile strength of ceramic material is generally far lower than compressive strength [49] and the metallic component tends to yield firstly before fracture, only the maximum principal stress of brittle components and equivalent stress of stainless frames/IC are shown. It could be seen that the thermal stress of cell with uniform temperature is distributed symmetrically in both width and length direction, which can be attributed to the symmetry of geometric structure, constrain condition and thermal load in both directions. However, the thermal stress is distributed symmetrically only in width direction for the IMSR stack, for the temperature distribution is only symmetric in width direction. The stress is relatively uniform for stack with constant temperature while highly uneven for stack with temperature difference, which is consistent with the previous result [24]. As shown in Fig. 5(a)(b), Fig. 6(a)(b), Fig. 7(a)(b) and Fig. 8(a)(b), the maximum stress values of anode, electrolyte, cathode and sealant are 19.6 MPa, 8.89 MPa, 11.4 MPa and 17.5 MPa, for isothermal stack and 33.2 MPa, 31.3 MPa, 23.7 MPa and 31.6 MPa for an operating stack. The maximum stress of corresponding components of an operating stack are respectively decreased by 40.9%, 63.6%, 51.9% and 45% when the thermal load is changed from the actual temperature distribution to the volume-averaged temperature. As shown in Fig. 9(a)(b), the maximum equivalent stress of frames/IC with uniform temperature is 33.1Mpa, about 1/3 of that of stack with uneven temperature. The corresponding failure probability of anode, electrolyte, cathode and sealant decreases from 1.20E-7, 6.73E-9, 4.30E-3 and 1 for an operating stack to 4.14E-11, 7.22E-13, 4.39E-4 and 7.36E-1 for stack with volume-averaged temperature. It can be seen clearly that the mechanical reliability and integrity are significantly affected by temperature

distribution. The results also clearly demonstrate that the previous studies using isothermal field underestimate the risks of mechanical failure of SOFC stacks.

As displayed in Fig. 5(a), the maximum stress of anode with uniform temperature is at all the orthogonal corners and the outer edge of the cuboid structure. However, the maximum stress of anode is located at corners of low-temperature area when loaded by thermal field of the IMSR stack, and the tensile stress in the high-temperature area decreases toward zero. For electrolyte and cathode shown in Fig. 6(a)(b) and Fig. 7(a)(b), larger stress is observed at the interface between different components and the outer edge. However, compared with isothermal stack, the location of the peak stress moves to high temperature outer edge in the IMSR stack. Besides, stress state is changed from compressive state to tensile state in partial high temperature area of electrolyte and cathode. Hence, the temperature distribution changes not only the locations of maximum stress, but also the stress state, which may shift from compressive stress state to tensile stress state or vice versa.

3.4 The influence of MSR pre-reforming ratio on stress distribution characteristic

Figures from Fig. 5 to Fig. 9 show the change of the maximum principal stress of PEN components and sealant and the equivalent stress of stainless frame/IC with the increase of R. As Fig. 4 shows, the lower part of IMSR SOFC stack has higher temperature while the upper part has lower temperature. For the low-temperature area of anode, the larger TEC and temperature difference from reference temperature lead to larger thermal contraction strain, then the thermal contraction is hindered by adjacent components and the high-temperature area of anode itself, thus tensile stress tends to appear. Accordingly, as shown in Fig. 5b, the high-temperature area of anode tends to be under lower tensile stress even compressive stress, which is induced by the “drag effect” of low temperature area of anode. With increasing R, the maximum principal stress of anode decreases overall. Both tensile stress and compressive stress can exist inside the same

anode layer when the overall temperature is high enough. For example, in addition to the presence of tensile stress, the compressive stress appears in high-temperature area for both stacks with R=0.4 and R=1. Although the stress distribution of anode is distinctively affected by temperature distribution overall, the local stress distribution change is not strictly consistent with temperature distribution, because the surrounding constrain can also influence the stress state significantly. When R increases from 0 to 0.4 then to 1, the maximum principal stress of anode decreases from 33.2 MPa to 24.0 MPa, and then to 13.3 MPa, decreasing by about 25% and 60%, respectively. The fracture strength of Ni-YSZ anode is in the range of 52-100 MPa [3], hence, the anode is always in safe state and the anode mechanical reliability tends to be improved with increasing R according to strength theory.

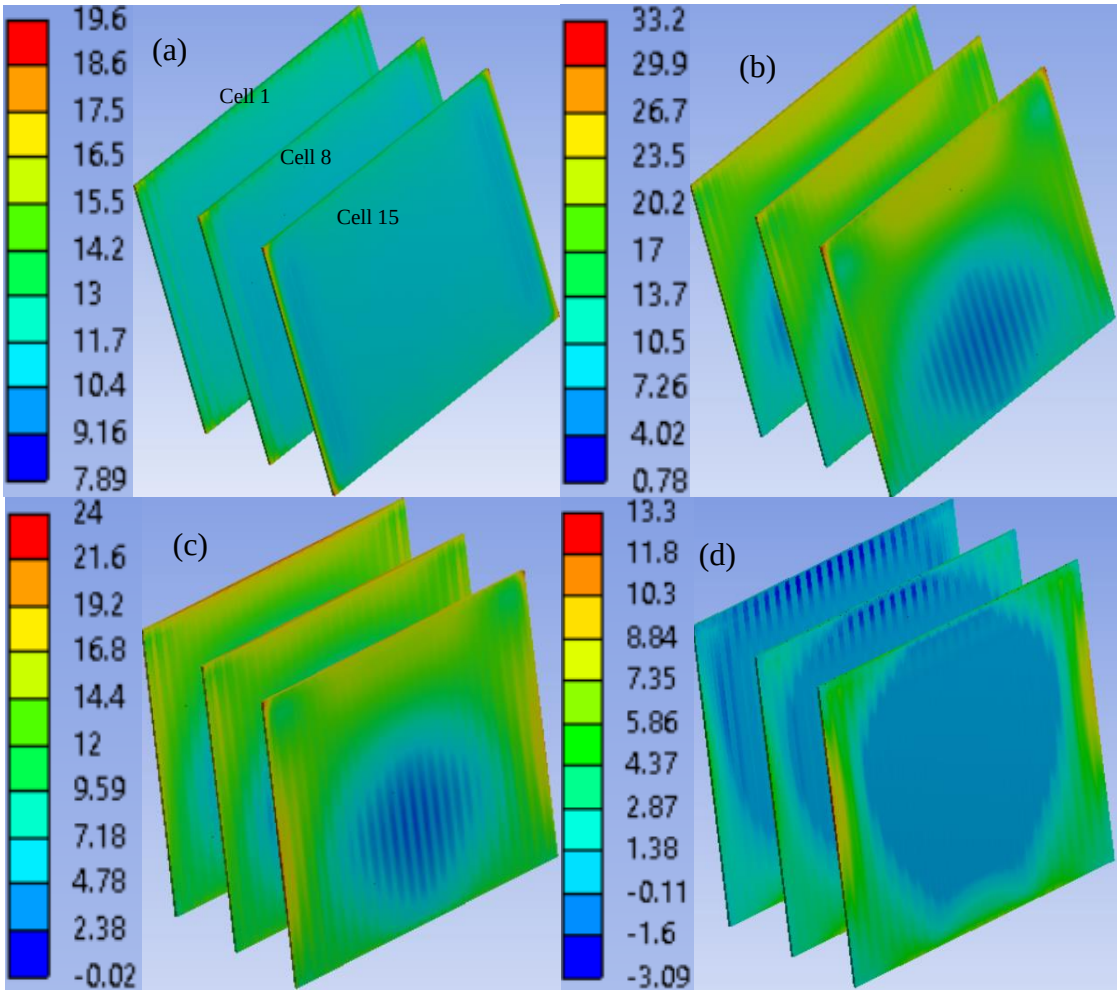

Fig. 5. The maximum principal stress (MPa) distribution of anode: (a) uniform temperature; (b)R=0; (c) R=0.4; (d) R=1.

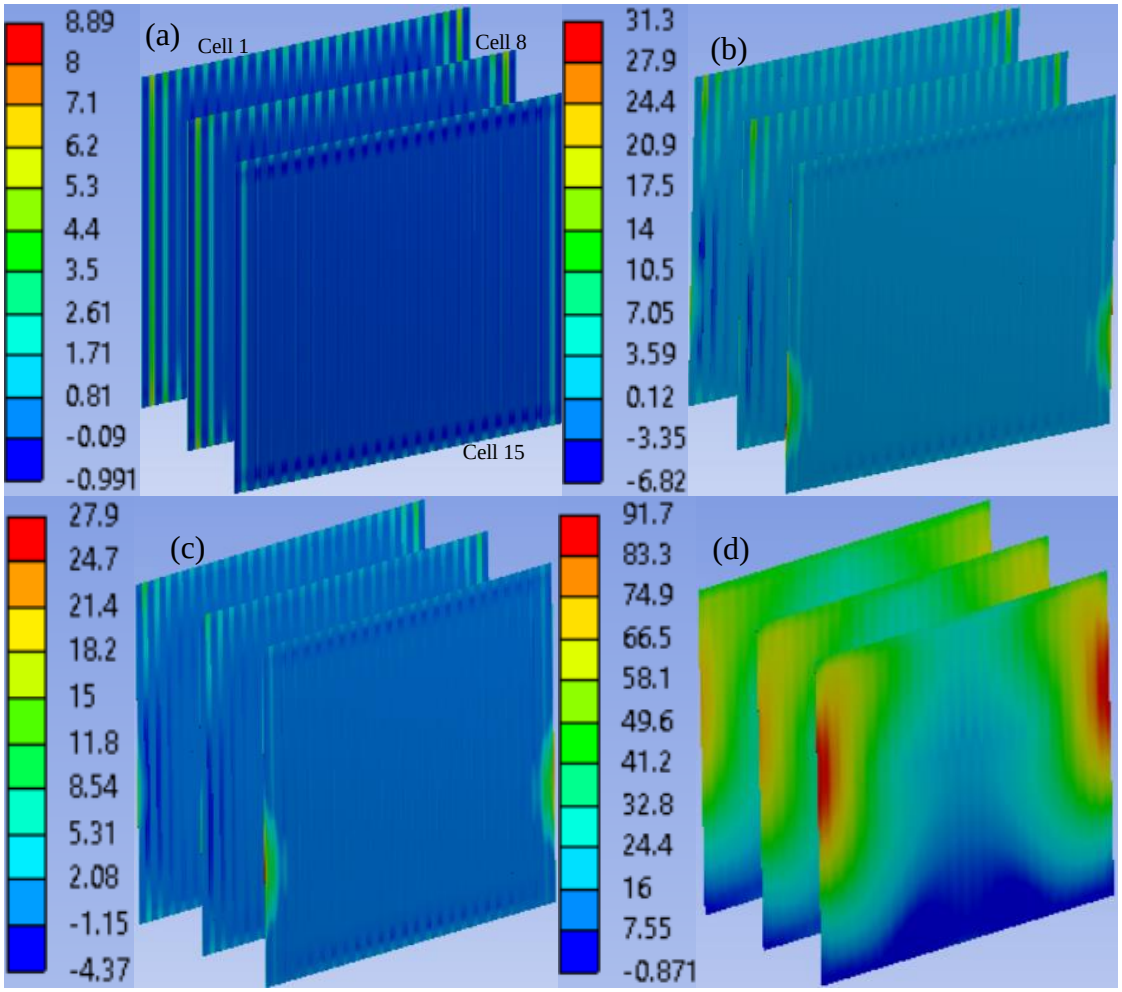

Fig. 6. The maximum principal stress (MPa) distribution of electrolyte: (a) uniform temperature; (b) R=0; (c) R=0.4; (d) R=1.

For electrolyte, it can be seen from Fig. 6 that both tensile and compressive stress coexist in the same electrolyte layer for stack loaded by either constant temperature or uneven temperature. The electrolyte in the isothermal SOFC stack tends to be compressive, due to its smallest thermal expansion coefficient and thinnest thickness compared with anode and cathode. When R increases from 0 to 0.4, the maximum tensile stress of electrolyte decreases from 31.3 MPa to 27.9 MPa, which can be ascribed to the decrease of temperature difference from reference temperature,

which finally leads to the decrease of thermal strain. When R increases from 0.4 to 1, the temperature continues to increase and the maximum temperature even exceeds the reference zero-stress temperature. The stretching effect from anode and cathode cause the electrolyte to expand more, hence, the compressive stress inside electrolyte is released dramatically, and the tensile stress of electrolyte increases significantly. When R increases from 0 to 1, the stress state of electrolyte changes from compressive state or lower tensile stress state to almost totally tensile stress state. The XRD experiment study on SOFC half-cell indicated that the compressive stress of electrolyte decreased with the increase of temperature, and the stress change tendency shown in Fig. 6 is consistent with the experiment result [32]. The lower-temperature region tends to be compressive while higher-temperature region tends to be stretched, totally opposite to that of anode. This can be ascribed to expansion under a high -temperature area and contraction under a low temperature area of anode, which correspondingly induce tension and compression of electrolyte in low and high temperature area, respectively. Compared with anode and cathode, the thinner thickness and larger Young's modulus of electrolyte makes it more sensitive to temperature variation, external load and effect from adjacent components, because only a small deformation can induce relatively larger strain, thus producing larger stress. Considering the ceramic generally has larger compressive resistance than tensile resistance [50], more attention should be paid to electrolyte when the SOFC stack is operated at the EMSR state.

It can be seen from Fig. 7(b)(c)(d) that the overall stress state of cathode has similar change trend to that of electrolyte. However, the maximum stress value decreases all the way when R value is changed from 0 to 0.4 and then to 1, which is similar to that of anode. This is because that the thickness and TEC of cathode are both between those of electrolyte and anode. With the increase of R, the maximum stress value decreases from 23.7 MPa to 16.5 MPa and then to 15.1 MPa, decreases by 30.3% and 36.3%, respectively. Besides, the stress distribution in most part of cathode changes from compressive state to tensile state especially in high temperature area, which

can also be ascribed to the stretching effect of anode.

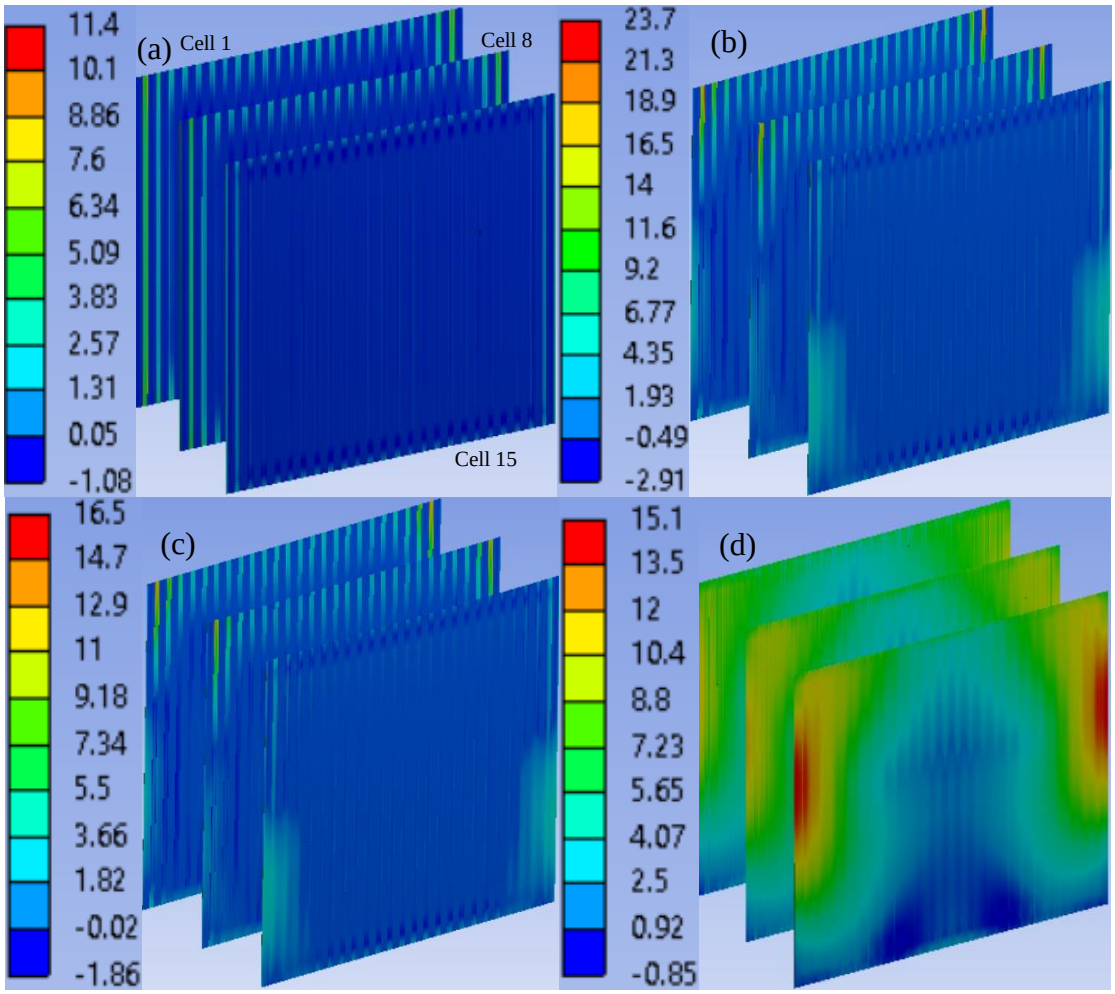

Fig. 7. The maximum principal stress (MPa) distribution of cathode: (a) uniform temperature; (b) R=0; (c) R=0.4; (d) R=1.

Fig. 8 displays the maximum principal stress distribution of sealant. Due to the strict constrain of internal and outer components, it is supposed that adjacent components can affect the stress distribution of sealant seriously. Comparing Fig. 8a and Fig. 8b, it can be seen that the peak principal stress value locates at the interface between sealant and adjacent components, no matter whether the thermal load is uniform or not. Besides, the peak stress also appears on the outer edge of sealant. The result is consistent with a previous numerical simulation [8] and in agreement with experimental observations [51]. As can be seen from Fig. 8(b)(c)(d), the maximum stress value of

sealant decreases all the way with the increase of R. However, it can also be seen that the area withstanding compressive stress decreases while area subjected to tensile stress increases, which means the compressive stress of sealant is released with the increase of R.

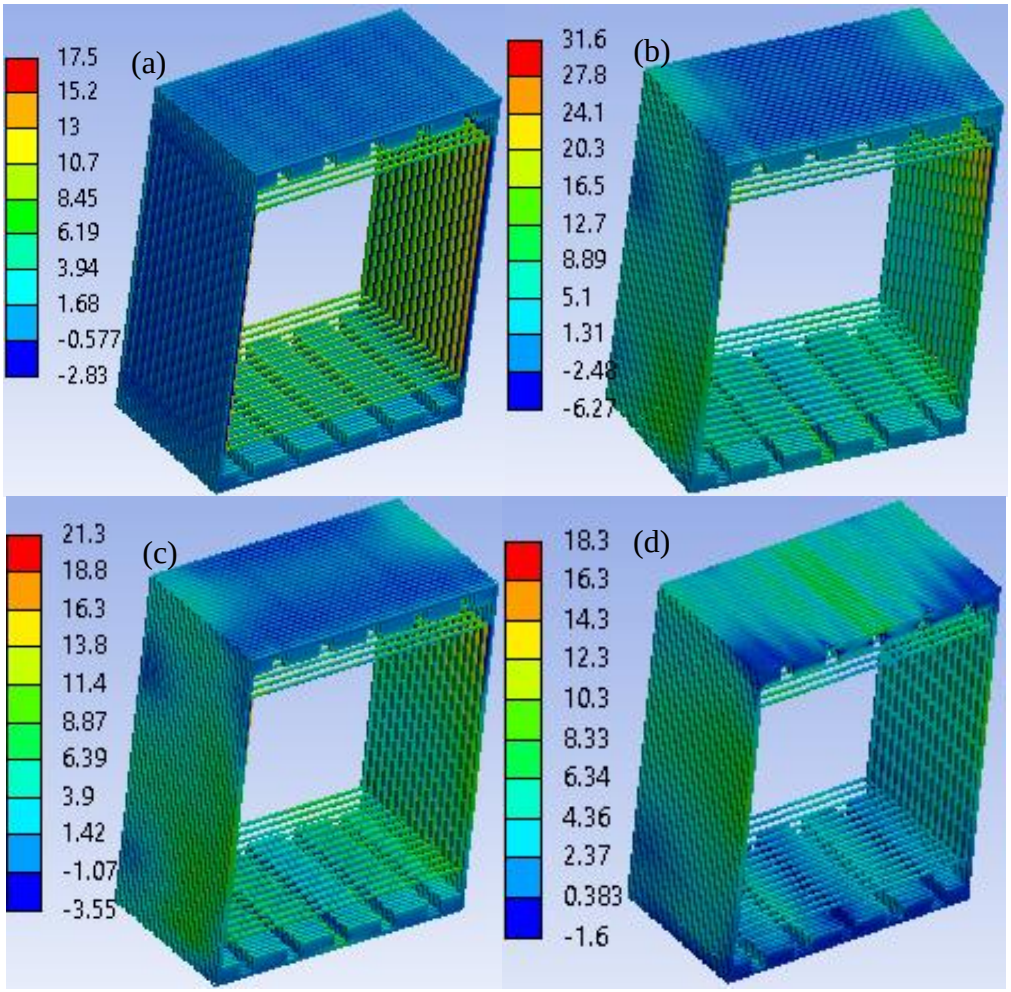

Fig. 8. The maximum principal stress (MPa) distribution of sealant: (a) uniform temperature; (b) R=0; (c) R=0.4; (d) R=1.

For metal alloy material, when the equivalent stress is larger than the elastic strength limit while lower than the fracture strength, the better ductility makes it firstly yield plastically rather than fracture like a brittle component. Plastic yielding and fracture can induce irreversible deformation and damage of component, leading to contact loose between adjacent components,

and thus causing gas leakage. The region of larger stress tends to be the area where potential plasticity yielding or fracture may occur. The equivalent stress distributions of metal frames are displayed in Fig. 9. Due to the model symmetry, only 1/2 of the metal frames is displayed for better visualization of the high stress locations that are emphasized by red circles in Fig. 9. As can be seen from Fig. 9, the maximum equivalent stress of metal alloy components decreases first then increases when R increases from 0 to 0.4 then to 1. The high stress area is located around the orthogonal corners of manifold inlets and outlets, which has also been reported in the simulation research [8]. Besides, the gas leakage around manifold inlet/outlet has also been observed experimentally [51]. It can be said that the simulation results of Fig. 9 have both the theoretical and experimental supports.

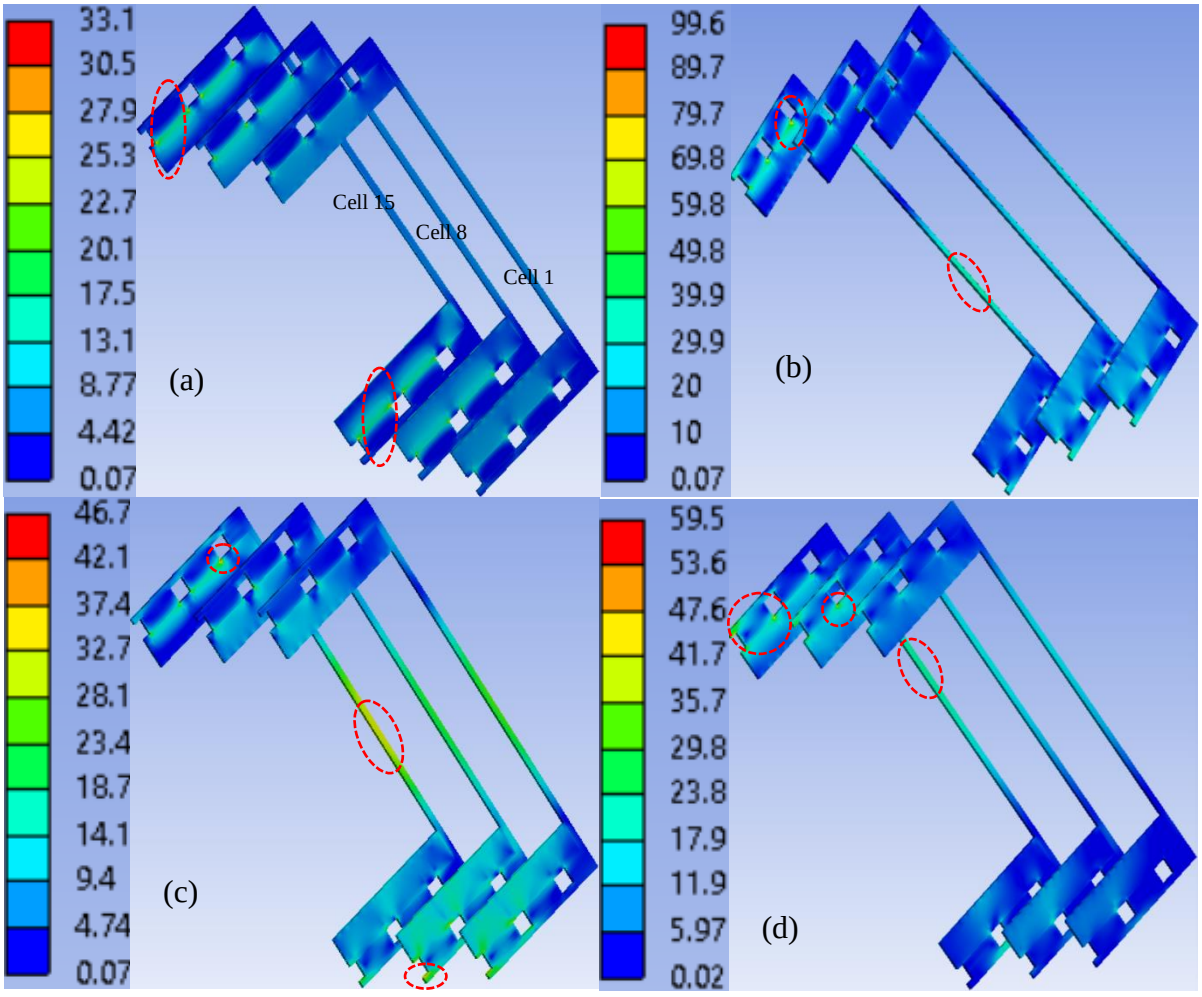

Fig. 9. Equivalent stress (MPa) of steel frames: (a) uniform temperature; (b) R=0; (c) R=0.4; (d) R=1.

As displayed in Fig. 9, as the larger stress around corners of manifold exist in both the isothermal stack (Fig. 9a) and operating stacks (Fig. 9(b)(c)(d)), it can be speculated that the larger stress around corners of manifolds is induced by the geometry and material properties' discontinuity rather than temperature gradient. Considering the second largest stress in the outer edge of frames (in Fig. 9(b)(c)(d)) does not appear in stack with constant temperature (Fig. 9a), it can be concluded that this potential failure location in Fig. 9(b)(c)(d) is induced by temperature unevenness. Notably, the maximum equivalent stress of frames/IC of stack with R=0 and R=0.4 is lower than plastic yield strength, while the maximum equivalent stress of stack with R=1 is only slightly higher than the plastic yield strength, the plastic strain is not considered here. Even so, the risk of plastic yield of metal frames tends to increase with the increases of R, therefore more attention should be paid to frames when EMSR is the operation mode. The research about plastic strain will be conducted in the subsequent study, which is not the focus of this study.

In summary, when R increases from 0 to 1, the most part of anode is in tensile stress state while changes from compressive stress state to tensile stress state for electrolyte, cathode and sealant. The maximum equivalent stress of frames/IC decreases first then increases, the risk of plastic yield of metal frames tends to increase with the increases of R.

3.5 The influence of MSR pre-reforming ratio on mechanical failure

The strength of brittle material is statistically distributed and size dependent, so failure probability analysis is more reasonable for risk assessment. Table 4 lists the failure probability of SOFC stack components when stack operates with different R. As can be seen, the failure probability decreases all the way for anode when R increases from 0 to 1, which is in accordance with tensile stress change shown in Fig. 5(b)(c)(d). When R increases, the temperature of SOFC

stack increases, the increased temperature and larger TEC cause anode to expand more or release much more contraction. However, the constraint from adjacent layers and low-temperature area of anode itself hinder its expansion or contraction release, thus leading to the decrease of tensile stress and the increase of compressive stress in anode. Consequently, the anode of IMSR stack has the maximum failure probability 1.2E-7, which is lower than the general engineering safety criterion 1E-6 [6, 40], therefore the anode is always in safe state for different R.

Different from the anode, the failure probability of electrolyte is small when temperature is relatively low. With the increase of R, the failure probability of electrolyte decreases first then increases, consistent with the stress change shown in Fig. 6(b)(c)(d). Only when R is as high as 0.7, the failure probability starts to exceed 1E-6. It seems that relatively lower temperature is preferable for electrolyte integrity, because electrolyte tends to be compressive when temperature is low. R not exceeding 0.7 is always suitable in view of the safety of electrolyte.

Similar to electrolyte, the failure probability of cathode also first decreases then increases. Though the maximum stress value of cathode decreases all the way, the overall stress state of cathode is changed from lower tensile stress to larger tensile stress state. When R is larger than 0.6, the failure probability starts to increase dramatically. For different R, the failure probability of cathode is always larger than 1E-3, which is larger than the engineering safety criterion of 1E-6. However, partially pre-reforming reaction still decreases the failure risk of cathode.

Table 4 Failure probability of brittle components

Case	Anode	Electrolyte	Cathode	Sealant
R=0	1.191E-7	6.731E-9	4.303E-3	1.000E+0
R=0.2	1.654E-8	4.946E-9	2.138E-3	9.996E-1
R=0.4	1.484E-9	3.020E-9	7.533E-4	8.051E-1
R=0.6	2.655E-11	1.1054E-7	4.723E-4	1.078E-1

R=0.8	1.635E-12	3.279E-6	1.901E-3	3.400E-2
R=1	8.971E-14	1.320E-3	3.224E-2	6.847E-2

When R increases from 0 to 0.2, the failure probability of sealant remains close to 1. When R increases from 0.2 to 0.8, the failure probability decreases gradually. However, when the temperature is high enough, the failure probability turns to increase. For R in the range of 0-1, the failure probability of sealant is always larger than 3E-2 and is always the largest among all the brittle components. Therefore, sealant is the component most susceptible to mechanical failure, which is consistent with the theoretical and experimental results in the literature [22, 45, 51]. The strict constrain of adjacent components makes sealant susceptible to temperature variation. Stress arises easily for a tightly bonded component rather than that with more freedom to deform. Above all, the sealing method should be improved to achieve better stack mechanical performance. However, even for rigid-sealed SOFC stack, the increased R can still improve the safety of sealant in a limited scope.

In summary, for R in the range 0-1, the failure probability of cathode and sealant is always larger than 1E-3 and 3E-2, respectively. By the failure probability analysis, it can be concluded that the glass-ceramic sealant is the most dangerous component and the cathode is in sub-critical state for R in the entire range 0-1. When $R<0.4$, the electrolyte has minimum failure probability. When $R\geq0.4$, anode becomes the safest component in SOFC stack and electrolyte has larger failure probability than anode. Compared with totally EMSR or totally IMSR operations, R lies in the range 0.4-0.7 is a good choice for the mechanical reliability of all the components of SOFC stack.

4. Conclusions

The thermo-mechanical model is developed to investigate the mechanical performance of the

15-cell SOFC stack. Cases covering all the range from the fully external methane steam reforming reaction, partially reforming reaction to fully internal reforming reaction are investigated. The influence of methane steam pre-reforming ratio (denoted as R) on SOFC mechanical performance are systematically evaluated. It finds out:

(1) Compared with the practical operating stack, the maximum principal stress of anode, electrolyte, cathode, sealant and the maximum equivalent stress of steel frames/IC of SOFC stack with uniform temperature is decreased by 41%, 71.6%, 52%, 49.8% and 66.8%, respectively. The corresponding failure probability of anode, electrolyte, cathode and sealant is decreased from 1.20E-7, 6.73E-9, 4.30E-3 and 1 for an operating stack to 4.14E-11, 7.22E-13, 4.39E-4 and 7.36E-1 for stack with volume-averaged temperature.

(2) Covering all R conditions, glass-ceramic sealant is the most dangerous component, while cathode is in sub-critical state among all components. When $R<0.4$, the electrolyte has minimum failure probability and is always in safe compressive stress scope. When $R\geq0.4$, anode becomes the safest component in SOFC stack and electrolyte has larger failure probability than anode. The anode is always in safe condition for R in range 0-1. Metal alloy frames have larger yielding risk for stack with larger R.

(3) For all the components, the mechanical reliability and integrity have been improved by methane steam pre-reforming reaction, while the security improvement of glass-ceramic sealant is quite limited, a superior sealing method may be an alternative. To keep R in the range of 0.4-0.7 is a better choice for the reliability of the whole SOFC stack.

Acknowledgement

The authors thank the financial support of the National Natural Science Foundation of China (12074362 & 11774324). The computing time at the Super-computing Center of University of Science and Technology of China is also greatly acknowledged. M. Ni thanks the financial

support from The Hong Kong Polytechnic University under the Project of Strategic Importance funding scheme (Project ID: P0035168).

References

[1] Ding, X., Lv, X., & Weng, Y. Coupling effect of operating parameters on performance of a biogas-fueled solid oxide fuel cell/gas turbine hybrid system. Appl. Energy 2019; 254:113675.

[2] Chen, B., Xu, H., Tan, P., Zhang, Y., Xu, X., Cai, W., Chen, M. & Ni, M. Thermal modelling of ethanol-fuelled Solid Oxide Fuel Cells. Appl. Energy 2019; 237:476-486.

[3] Anandakumar, G., Li, N., Verma, A., Singh, P., & Kim, J. H. Thermal stress and probability of failure analyses of functionally graded solid oxide fuel cells. J. Power Sources 2010; 195:6659-6670.

[4] Lin, C. K., Huang, L. H., Chiang, L. K., & Chyou, Y. P. Thermal stress analysis of planar solid oxide fuel cell stacks: Effects of sealing design. J. Power Sources 2009; 192:515-524.

[5] Lin, C. K., Chen, T. T., Chyou, Y. P., & Chiang, L. K. Thermal stress analysis of a planar SOFC stack. J. Power Sources 2007; 164:238-251.

[6] Fang, X., Zhu, J., & Lin, Z. Effects of electrode composition and thickness on the mechanical performance of a solid oxide fuel cell. Energies 2018; 11:1735.

[7] Montross, C. S., Yokokawa, H., & Dokiya, M. Thermal stresses in planar solid oxide fuel cells due to thermal expansion differences. Br Ceram Trans 2002; 101:85-93.

[8] Peksen, M. A coupled 3D thermofluid-thermomechanical analysis of a planar type production scale SOFC stack. Int. J. Hydrogen Energy 2011;36: 11914-11928.

[9] Li, A., Song, C., & Lin, Z. A multiphysics fully coupled modeling tool for the design and operation analysis of planar solid oxide fuel cell stacks. Appl. Energy 2017; 190:1234-1244.

[10] Miao, X. Y., Rizvandi, O. B., Navasa, M., & Frandsen, H. L. Modelling of local mechanical failures in solid oxide cell stacks. Appl. Energy 2021; 293:116901.

[11] Xia, W., Yang, Y. & Wang, Q. Effects of operations and structural parameters on the one-cell stack performance of planar solid oxide fuel cell. J. Power Sources 2009; 194: 886-898.

[12] Zhang, Z., Yue, D., Yang, G., Chen, J., Zheng, Y., Miao, H., Wang, W., Yuan, J., & Huang, N. Three-dimensional CFD modeling of transport phenomena in multi-channel anode-supported planar SOFCs. Int. J. Heat Mass Transf 2015; 84:942–954.

[13] Guo, M., Xiao, G., Wang, J., & Lin, Z. Parametric study of kW-class solid oxide fuel cell stacks fueled by hydrogen and methane with fully multiphysical coupling model. Int. J. Hydrogen Energy 2021; 46:9488-9502.

[14] Eveloy, V. Anode gas and steam recycling for internal methane reforming SOFCs: Analysis of carbon deposition. ASME Int. Mech. Eng. Congr. Expo. Proc 2010; 6:627-639.

[15] Lee, K., Kang, S., & Ahn, K. Y. Development of a highly efficient solid oxide fuel cell system. Appl. Energy 2017; 205:822-833.

[16] Yun, J., & Yu, S. Transient behavior of 5 kW class shell-and-tube methane steam reformer with intermediate temperature heat source. Int. J. Heat Mass Transf 2019; 134:600-9.

[17] Kang, S., Lee, K., Yu, S., Lee, S. M. & Ahn, K. Y. Development of a coupled reactor with a catalytic combustor and steam reformer for a 5 kW solid oxide fuel cell system. App. Energy 2014; 114:114-123.

[18] Koo, T., Kim, Y. S., Lee, Y. D., Yu, S., Lee, D. K., & Ahn, K. Y. Exergetic evaluation of operation results of 5-kW-class SOFC-HCCI engine hybrid power generation system. Appl. Energy 2021; 295:117037.

[19] Ghang, T. G., Lee, S. M., Ahn, K. Y., & Kim, Y. An experimental study on the reaction characteristics of a coupled reactor with a catalytic combustor and a steam reformer for SOFC systems. Int J Hydrogen Energy 2012; 37:3234–41.

[20] Nishida, R. T., Beale, S. B., Pharoah, J. G., de Haart, L. G. J. & Blum, L. Three-dimensional computational fluid dynamics modelling and experimental validation of the Jülich Mark-F solid oxide fuel cell stack. J. Power Sources 2018; 373:203-210.

[21] Frandsen, H. L., Makowska, M., Greco, F., Chatzichristodoulou, C., Ni, D. W., Curran, D. J., Strobl, M., Kuhn, L. T., & Hendriksen, P. v. Accelerated creep in solid oxide fuel cell anode supports during reduction. J. Power Sources 2016; 323:78-89.

[22] Wang, Y., Jiang, W., Luo, Y., Zhang, Y., & Tu, S. T. Evolution of thermal stress and failure probability during reduction and re-oxidation of solid oxide fuel cell. J. Power Sources 2017; 371:65-76.

[23] Hashin, Z., & Shtrikman, S. A variational approach to the theory of the elastic behavior of multiphase materials. J. Mech Phys Solid 1963; 11:127-40.

[24] Guo, M., & Lin, Z. Long-term evolution of mechanical performance of solid oxide fuel cell stack and the underlying mechanism analysis. Int. J. Hydrogen Energy 2021; 46:24293-24304.

[25] Ramakrishnan, N., & Arunachalam, V. S. Effective elastic moduli of porous solids. J. MATERIALS SCIENCE 1990; 25:3930-3937.

[26] Kerner, E. H. The Elastic and Thermo-elastic Properties of Composite Media. Proc. Phys. Soc 1956; Section B:808-813.

[27] Mori, M., Yamamoto, T., & Itoh, H. Thermal Expansion of Nickel-Zirconia Anodes in Solid Oxide Fuel Cells during Fabrication and Operation. J. Electrochem. Soc 1998; 145:1373.

[28] Fischer, H., Rentzsch, W., & Marx, R. A modified size effect model for brittle nonmetallic materials. Eng Fract Mech 2002; 69:781-791.

[29] Laurencin, J., Delette, G., Lefebvre-Joud, F., & Dupeux, M. A numerical tool to estimate SOFC mechanical degradation: Case of the planar cell configuration. J. Eur Ceram Soc 2008; 28:1857-1869.

[30] Zhang, T., Zhu, Q., Huang, W. L., Xie, Z., & Xin, X. Stress field and failure probability analysis for the single cell of planar solid oxide fuel cells. J. Power Sources 2008; 182:540-545.

[31] Wei, J., & Malzbender, J. Steady state creep of Ni-8YSZ substrates for application in solid oxide fuel and electrolysis cells. J. Power Sources. 2017; 360:1-10.

[32] Malzbender J, Fischer W, Steinbrech RW. Studies of residual stresses in planar solid oxide fuel cells. J. Power Sources 2008;182: 594–8.

[33] Fischer, W., Malzbender, J., Blass, G. & Steinbrech, R. W. Residual stresses in planar solid oxide fuel cells. J. Power Sources. 2005; 150:73-77.

[34] Radovic, M., & Lara-Curzio, E. Elastic properties of Nickel-Based Anodes for Solid Oxide Fuel Cells as a Function of Fraction of Reduced NIO[J]. J. Am. Ceram. Soc 2004; 87:2242-6.

[35] Fang, X., & Lin, Z. Numerical study on the mechanical stress and mechanical failure of planar solid oxide fuel cell. Appl. Energy 2018; 229:63-68.

[36] Hubert, O., Milhet, X., Gadaud, P., Tatat, M., Renault, P. O., & Coupeau, C. Modeling of Young's modulus variations with temperature of Ni and oxidized Ni using a magneto-mechanical approach. Mater. Sci. Eng 2015; A 633:76-91.

[37] Nakajo, A., Wuillemin, Z., van herle, J., & Favrat, D. Simulation of thermal stresses in anode-supported solid oxide fuel cell stacks. Part I: Probability of failure of the cells. J. Power Sources 2009;193(1):203-215.

[38] Dunand, D. C., Han, B. Q., & Jansen, A. M. Monkman-grant analysis of creep fracture in dispersion-strengthened and particulate-reinforced aluminum. Metall Mater Trans A 1999; 30:829-838.

[39] Cutler, R. A. & Meixner, D. L. Ceria-lanthanum strontium manganite composites for use in oxygen generation systems. Solid State Ionics. 2003; 159:9–19.

[40] Li, J., & Lin, Z. Effects of electrode composition on the electrochemical performance and mechanical property of micro-tubular solid oxide fuel cell. Int. J. Hydrogen Energy 2012;37: 12925-12940.

[41] Basu, R. N., Tietz, F., Teller, O., Wessel, E., Buchkremer, H. P., & Stöver, D. LaNi0.6Fe0.4O3 as a cathode contact material for solid oxide fuel cells. J. Solid State Electrochem 2003; 7:416-420.

[42] Greco, F., Frandsen, H. L., Nakajo, A., Madsen, M. F., & van herle, J. Modelling the impact of creep on the probability of failure of a solid oxide fuel cell stack. J. Eur. Ceram. Soc 2014; 34:2695-2704.

[43] Ni, D. W., Charlas, B., Kwok, K., Molla, T. T., Hendriksen, P. V., & Frandsen, H. L. Influence of temperature and atmosphere on the strength and elastic modulus of solid oxide fuel cell anode supports. J. Power Sources 2016; 311:1-12.

[44] Nakajo, A., Kuebler, J., Faes, A., Vogt, U. F., Schindler, H. J., Chiang, L. K., Modena, S., van Herle, J., & Hocker, T. Compilation of mechanical properties for the structural analysis of solid oxide fuel cell stacks. Constitutive materials of anode-supported cells. Ceram. Int 2012; 38:3907-3927.

[45] Jiang, W., Luo, Y., Zhang, W., Woo, W., & Tu, S. T. Effect of Temperature Fluctuation on Creep and Failure Probability for Planar Solid Oxide Fuel Cell. J. Fuel Cell Sci Technol 2015; 12:51004.

[46] Vaidya, S., & Kim, J. H. Finite element thermal stress analysis of solid oxide fuel cell cathode microstructures. J. Power Sources 2013; 225:269-276.

[47] Nakajo, A., Mueller, F., Brouwer, J., van Herle, J., & Favrat, D. Mechanical reliability and durability of SOFC stacks. Part I: Modelling of the effect of operating conditions and design alternatives on the reliability. Int. J. Hydrogen Energy 2012; 37:9249-9268.

[48] Bi, W., Chen, D. & Lin, Z. A key geometric parameter for the flow uniformity in planar solid oxide fuel cell stacks. Int. J. Hydrogen Energy 2009; 34:3873-3884.

[49] Laurencin, J., Delette, G., Usseglio-Viretta, F., & di Iorio, S. Creep behaviour of porous SOFC electrodes: Measurement and application to Ni-8YSZ cermets. J. Eur. Ceram. Soc 2011; 31:1741-1752.

[50] Liu, X., Martin, C. L., Bouvard, D., di Iorio, S., Laurencin, J., & Delette, G. Strength of highly porous ceramic electrodes. J. Am. Ceram. Soc 2011; 94:3500-3508.

[51] Peksen, M. 3D thermomechanical behaviour of solid oxide fuel cells operating in different environments. Int. J. Hydrogen Energy 2013; 38:13408-13418.